



**HAL**  
open science

## A robust multi-variability model based liver segmentation algorithm for CT-scan and MRI modalities

Marie-Ange Lebre, Antoine Vacavant, Manuel Grand-Brochier, Hugo Rositi, Robin Strand, Hubert Rosier, Armand Abergel, Pascal Chabrot, Benoît Magnin

### ► To cite this version:

Marie-Ange Lebre, Antoine Vacavant, Manuel Grand-Brochier, Hugo Rositi, Robin Strand, et al.. A robust multi-variability model based liver segmentation algorithm for CT-scan and MRI modalities. Computerized Medical Imaging and Graphics, 2019, 76, pp.101635. 10.1016/j.compmedimag.2019.05.003 . hal-03164259

**HAL Id: hal-03164259**

**<https://uca.hal.science/hal-03164259>**

Submitted on 25 Oct 2021

**HAL** is a multi-disciplinary open access archive for the deposit and dissemination of scientific research documents, whether they are published or not. The documents may come from teaching and research institutions in France or abroad, or from public or private research centers.

L'archive ouverte pluridisciplinaire **HAL**, est destinée au dépôt et à la diffusion de documents scientifiques de niveau recherche, publiés ou non, émanant des établissements d'enseignement et de recherche français ou étrangers, des laboratoires publics ou privés.



Distributed under a Creative Commons Attribution - NonCommercial 4.0 International License

# A robust multi-variability model based liver segmentation algorithm for CT-scan and MRI modalities

Marie-Ange Lebre<sup>a</sup>, Antoine Vacavant<sup>a</sup>, Manuel Grand-Brochier<sup>a</sup>, Hugo Rositi<sup>a</sup>, Robin Strand<sup>b</sup>, Hubert Rosier<sup>c</sup>, Benoît Magnin<sup>a</sup>, Armand Abergel<sup>a</sup>, Pascal Chabrot<sup>a</sup>

<sup>a</sup>Université Clermont Auvergne, CHU Clermont-Ferrand, CNRS, SIGMA Clermont, Institut Pascal, F-63000 Clermont-Ferrand, France

<sup>b</sup>Centre for Image Analysis, Uppsala University, Sweden

<sup>c</sup>Centre Hospitalier Émile Roux, Le Puy-en-Velay, France.

## Abstract

Developing methods to segment the liver in medical images, study and analyze it remains a significant challenge. The shape of the liver can vary considerably from one patient to another, and adjacent organs are visualized in medical images with similar intensities, making the boundaries of the liver ambiguous. Consequently, automatic or semi-automatic segmentation of liver is a difficult task. Moreover, scanning systems and magnetic resonance imaging have different settings and parameters. Thus the images obtained differ from one machine to another. In this article, we propose an automatic model-based segmentation that allows building a faithful 3-D representation of the liver, with a mean Dice value equal to 90.3% on CT and MRI datasets. We compare our algorithm with a semi-automatic method and with other approaches according to the state of the art. Our method works with different data sources, we use a large quantity of CT and MRI images from machines in various hospitals and multiple DICOM images available from public challenges. Finally, for evaluation of liver segmentation approaches in state of the art, robustness is not adequately addressed with a precise definition. Another originality of this article is the introduction of a novel measure of robustness, which takes into account the liver variability at different scales.

**Keywords:** Automatic segmentation, 3-D, liver, CT, MRI, shape model, variability, robustness.

## 1. Introduction

Surgery, oncology, radiotherapy, morphological studies and anatomy are examples of applications that require image segmentation. In medical images, problems affecting segmentation methods are noise, overlapping or fuzzy contours, highly variable shapes and appearances, complex backgrounds (organs and tissues with similar intensities and shapes) and low contrast. Liver segmentation is still a challenging task and attracts much attention from researchers. There are three main methods to address segmentation of the liver: classification methods, active contour detection and model-based methods. Classification methods consist of grouping individual components of the image such as pixels or sub-images and exploiting their similarities as opposed to the contour approach seeking dissimilarities, while model based methods can be statistical or supported by an atlas. Region growing methods [1], [2], histograms with thresholds [3], voxel classification algorithms [4], and graph cuts [5] are widely used as classification methods to segment the liver, but they often lead to over-segmentation problems [6]. In the contour approaches, some researchers improve the existing methods, for example Shi *et al.* [7] and Liu *et al.* [8] present improved deformable shape and contour models respectively. Several researches have improved this active contour based work by adding a signed force function to segment liver from MRIs [9, 10, 11]. Soler *et al.* [12] translate anatomical knowledge into topological and geometrical constraints with

the use of deformable models. Yang *et al.* [13] customize a fast marching level-set method.

Other methods are based on statistical models to deal with segmentation problems [14]. Massoptier *et al.* [15] propose a statistical model-based approach combined with an active contour technique using a gradient vector flow to obtain an automatic liver segmentation. Farzaneh *et al.* [16] propose a hierarchical method based on probabilistic models of position and intensity of voxels. Among these statistical models, Active Appearance Model (AAM) and Active Shape Model (ASM) have been widely used as high-level techniques in computer vision and image processing [17], [18]. An AAM allows to match a statistical model of object shape and appearance to a new image and ASM is a statistical model of the shape of objects, which iteratively deforms to fit to an example of the object in a new image. Dreuw *et al.* [19] introduce the use of appearance-based features in hidden Markov model emission probabilities to recognize dynamic gestures. They use tangent distance and image distortion to directly model image variability in videos on the German finger-spelling alphabet. Merck *et al.* [20] propose a method to jointly estimate both the geometric model for any given image and the shape distribution for the entire population of training images. Their method iteratively relax geometric constraints in favor of the converging shape probabilities as the fitted objects converge to their target segmentations. Rodzik *et al.* [21] assume a training set of images in which corresponding "landmark"

points have been marked in every images. From this data, they compute a statistical model of the shape variation, a model of the texture variation and a model of the correlations between shape and texture. Then, they find the parameters that optimize the matching operation. Ivekovic *et al.* [22] use a pyramid of statistical models to segment the input image on various resolution levels. After that, they apply a coefficient propagation through the Gaussian image pyramid and use one statistical model to perform the segmentation. Back in the context of liver segmentation, He *et al.* [23] present a three-level ASM. They first use a voxel classification step and then apply an ASM-constrained mesh model only on CT scans. Wimmer *et al.* [24] present an implicit ASM with a boundary classifier to guide the model. Linguraru *et al.* [25] propose a combination of appearance, enhancement and shape statistics to segment the liver. Okada *et al.* [26] present a probabilistic atlas and an ASM to automatically segment the liver. Moghbel *et al.* [27] propose a random walker based framework. Statistical models based on appearance or shape are parametric, they thus need to optimize the parameters and a good initialization to obtain proper convergence. More recently, deep learning has been used to automatically segment the liver on CT scans [28, 29] or on MRI [30].

Current automatic segmentation methods focused on the liver are not applied on a large variety of data acquisition conditions and they do not provide a 3-D representation. Besides this limited evaluation of liver segmentation approaches, their robustness is not properly addressed, with a clear definition of this important notion, related to the concrete use and reproducibility of image processing algorithms. Finally, it exists few studies on liver segmentation for both medical imaging modalities: CT scans and MRI. Gotra *et al.* [31] and Chartrand *et al.* [32] base their method on Laplacian mesh optimization. Suzuki *et al.* [33] use a fast marching and geodesic active contour segmentation coupled with level-set algorithms to segment on both modalities. Heinrich *et al.* [34] present an automatic multi-organ segmentation based on a discrete registration framework. Christ *et al.* [35] use a cascaded fully convolutional neural networks to segment liver and tumors.

Two major contributions compose our article. In the first one, we propose a robust, generic and efficient automatic segmentation algorithm using a model based on the liver shape variability to construct a 3-D representation of any patient’s liver. Our model is not parametric and does not need any parameter optimization scheme. Instead, we accumulate knowledge about the liver shape and its variability into a single representation from databases. Researchers develop liver segmentation in CT, but it exists fewer studies on MRI, while the latter modality arouses a lot of interest in clinical routine for oncology and diagnosis. Our method can extract the organ from different modalities: MRI and CT scan acquired in different places from different machines with different acquisition settings. Our second contribution is the introduction of a novel measure of robustness. Indeed, robustness is not properly and clearly defined in segmentation evaluations. Our measure is based on multiple scales of shape variability, as an extension of [36].

The paper is organized as follows: datasets and construction of the model based on the liver’s variability, are described in Section 2. Our approach is defined in Section 3 with the 3-D reconstruction process. Section 4 presents the novel robustness measurement. Section 5 discusses the numerical results we obtain, compared with other methods from state of the art, and in deep with the only other algorithm whose code is freely available, SmartPaint [37]. We also evaluate the robustness of both approaches, confirming the efficiency of our method. This section also provides numerous visual results for CT and MRI volumes, to appreciate this accuracy. Perspectives and conclusions are depicted in Section 6.

## 2. Materials description and shape model construction

Our method is based on a shape variability model of the liver. In this section, we present patient’s datasets used for the construction of this model, which is explained in Section 2.2.

### 2.1. Patient datasets

This study was performed from different sources of datasets. The first one comes from the statistical shape model challenge, Shape 2015 [38]. Among liver segmentations as binary MetaImage format images from anonymous patients, we selected 28 liver masks where  $X$ -dimensions are equal to  $Y$ -dimensions, 3-D images are isotropic with  $322-500 \times 322-400 \times 141-273 \text{ mm}^3$ . Medical examinations are not available in the Shape2015 database. The second one comes from the Research Institute against Digestive Cancer (IRCAD) [39]. We have access to medical images in DICOM format from 20 patients (10 men and 10 women). Image sizes are  $512 \times 512 \times 91-260 \text{ mm}^3$ , with the following voxel size:  $0.56-0.87 \times 0.56-0.87 \times 1.25-4 \text{ mm}^3$ . The 2007 liver segmentation competition (SLIVER) [40] provides another dataset. The contest goal was to compare different algorithms used to segment livers from 3-D CT scans. Image sizes are  $512 \times 512 \times 64-394 \text{ mm}^3$ , with the following voxel size:  $0.57-0.87 \times 0.57-0.87 \times 0.7-5 \text{ mm}^3$ .

Collaborations with clinicians made possible to obtain 40 MRI volumes directly from patients in two French Hospitals. MR exams were performed on different machines (General Electric Healthcare and Siemens) with a phased array coil. Image sizes are  $250-512 \times 320-512 \times 56-128 \text{ mm}^3$ , with the following voxel size:  $0.82-1.40 \times 0.82-1.40 \times 1.8-3 \text{ mm}^3$ . They have different sequences taken at different times in DICOM format. In this study, we use only the delayed phase: 3-5 minutes after contrast agent injection, because according to the medical expert, the contour of the liver is the most visible on this phase. Then, these MRI volumes come from patients with cirrhosis and cancer such as HCC (Hepatocellular Carcinoma). In case of liver disease, segmenting liver becomes a challenging task because the quality decreases considerably with more heterogeneous liver tissue density, moreover livers are severely deformed by the disease. In conclusion, our method works well in MRI and CT images of patients from different machines. We use a very large quantity of data from different sources, some are open-source from public websites (Shape2015, IRCAD and SLIVER) and other anonymized private data come from our

hospital departments. This shows the large quantity and the high variability of our datasets with 68 CT and 40 MRI images.

## 2.2. Shape models

The first step of our method is the construction of several shape models based on 68 CT volumes where liver is manually delineated. Each 3-D segmentation image has its own  $X$ ,  $Y$  and  $Z$  pixel spacing (see Section 2.1). These dimensions have to be uniformized for all the images to aggregate all of them in a single model. After a 3-D cubic interpolation, all 68 segmentations have the same spacing dimensions of  $X$ ,  $Y$  and  $Z$ , which is one millimeter pixel size. These values allowed imaging the real dimensions of the liver and processing further any new data. Then, we compute the mean 3-D gravity center of the liver:  $GV$  on these 68 segmentations. We also construct a bounding box with standard dimensions of the liver (in millimeters) certified by an expert and computed by the mean values of our database. The bounding box, denoted by  $BB$ , is used as a reference on each set of 3-D segmentations noted  $M_{j \in \{1,m\}}$ . It enables us to organize our liver data, depending on their variability, in four sets  $S_k = \{M_{j \in \{1,m\}}\}_k$  with  $k \in \{1, 4\}$ . Liver sets are defined according to their variability, *i.e.* the percentage of pixels that belong to the liver measured outside the  $BB$ . We denote by  $\sigma_M$  the variability measure of a binary segmentation  $M_{j \in \{1,m\}}$ , defined by:

$$\sigma_M = \frac{\text{Card}(L_M \setminus BB)}{\text{Card}(L_M)} \times 100 \quad (1)$$

$L_M$  is the set of pixels that belong to the liver in a binary segmentation  $M_{j \in \{1,m\}}$  and  $\text{Card}(L_M)$  is its cardinality.  $L_M \setminus BB$  thus represents pixels that belong to the liver measured outside the box  $BB$  and  $\text{Card}(L_M \setminus BB)$  is the cardinality of this set. We construct four liver sets thanks to this variability measure:

$$\begin{aligned} S_1 &= \{M_{j \in \{1,m\}}, 0\% \leq \sigma_M < 2\%\} \\ S_2 &= \{M_{j \in \{1,m\}}, 2\% \leq \sigma_M < 6\%\} \\ S_3 &= \{M_{j \in \{1,m\}}, 6\% \leq \sigma_M < 8\%\} \\ S_4 &= \{M_{j \in \{1,m\}}, \sigma_M \geq 8\%\} \end{aligned} \quad (2)$$

$S_1$  gathers the smallest livers,  $S_2$  and  $S_3$  represents livers slightly larger than the  $BB$  and  $S_4$  livers bigger than the  $BB$ . In each set  $S_k$ , we align the 3-D gravity center of all  $M_{j \in \{1,m\}}$  with the 3-D gravity center of the  $BB$  ( $GV$ ). This manipulation permits to center liver segmentations uniformly in space. After this positioning, we construct on each 2-D slice a probability map to evaluate the liver's presence. We obtain one volume for each  $S_k$ , we note them  $\mathbb{M}_k = \bar{M}_{j \in \{1,m_k\}}$ , a pixel value  $\bar{M}(s, t) \in [0, 1]$  in a  $j$ -slice is defined by:

$$\bar{M}(s, t) = \frac{1}{m_k} \sum_{n=1}^{m_k} M(s, t) \quad (3)$$

As the images are isotropic, dimensions are different between each  $M$ , therefore for each  $\mathbb{M}_k$ ,  $X$ -dimension,  $Y$ -dimension and  $Z$ -dimension correspond to the maximum dimensions in the group  $S_k = \{M_{j \in \{1,m\}}\}_k$ , so  $m_k = \max\{m, M_{j \in \{1,m\}} \in S_k\}$ . If the  $j$ -slice does not exist in one of a volume  $M_{j \in \{1,m\}}$  in  $S_k$ ,

we consider a background instead with  $M(s, t) = 0$ . Our models aggregate knowledge on shapes of the liver and do not need parameters optimization. Figure 1 shows this probability map obtained on one slice for each group.

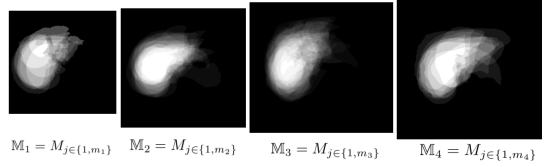


Figure 1: Probability map for one slice of  $\mathbb{M}_k$  with  $k \in \{1, 4\}$

Shape models were built with 68 manual segmentations. We obtain a probability map that reflects a standard position of the liver, we employ a rigid alignment to preserve invariants of pose that allows to take into account different positions. In the experimentation, some testing data are part of a shape model, to avoid bias we remove them in the shape model chosen.

## 3. Liver segmentation

Our method is composed of two steps based on these shape models. The following section is organized around these two points: first, we find the slice with the most significant surface of the liver thanks to the mean bounding box ( $BB$ ) to apply a threshold and select the region of interest on all medical images of a patient. Then, after using different filters, we use a fast marching method and an adjustment process to obtain a faithful 3-D reconstruction of the liver of the patient.

Let  $P_{j \in \{1,p\}}$  be these  $p$  medical images of a patient (CT or MRI modality (an exclusive-or)). Usually, images have anisotropic dimensions. Therefore we first proceed to a cubic interpolation to obtain uniform pixel spacing (1 mm).

### 3.1. Thresholding and area selection

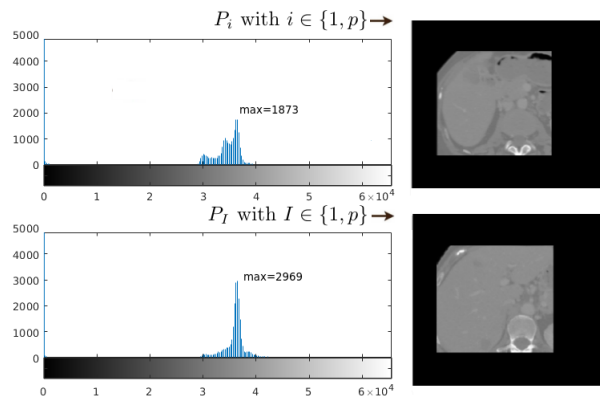


Figure 2: Intensity histogram evaluated in the  $BB$  on 2 patient images

The  $BB$  provides an approximate position of the liver within the volume. We crop this volume on the dataset  $P_{j \in \{1,p\}}$ . Then we compute the intensity histogram to find the 2-D image  $P_I$

with  $I \in \{1, p\}$ , where the largest surface of the liver. Thanks to the  $BB$ , lot of pixels belong to the liver and have similar intensities, therefore the slice with the largest liver surface has an intensity histogram with the highest peak. Figure 2 shows two intensity histograms at different slices on the slices:  $P_i$  as an example and  $P_l$  with the most substantial liver surface.

Then, by uniformizing pixel spacing, we can observe that the images of the different shape models of the liver  $\mathbb{M}_k$  have an increasing resolution according to the size of the liver (see Figure 1). This allows us to choose the shape model for the segmentation of the patient images  $P_{j \in \{1, p\}}$ . Indeed, we find the image  $\bar{M}_{J_1}$  with  $J_1 \in \{1, m_1\}$  with the maximum binary area of the first shape model  $\mathbb{M}_1$ . We note  $R(P_I)$  the resolution (number of pixels in  $X$  is equal to the number of pixels in  $Y$ ) of the image  $P_I$ , and  $R(\bar{M}_{J_1})$  the resolution of the image  $\bar{M}_{J_1}$ , if the condition (4) is false it means that the shape model  $\mathbb{M}_k = \mathbb{M}_1$  is too small, so we test the condition on the model with a superior  $k$ :

$$R(P_I) \leq R(\bar{M}_{J_k} \in \mathbb{M}_k). \quad (4)$$

Once  $k$  is chosen, we apply  $\bar{M}_{J_k}$  as a mask on  $P_I$  by considering pixels with a probability higher than a fixed percentage called  $\beta_1$  on the shape model, the image obtained is noted  $P_I$  (Figure 3). We consider  $D$  the pixels intensity distribution of  $P_I$  with  $\mu$  the mean and  $\delta$  the standard deviation.

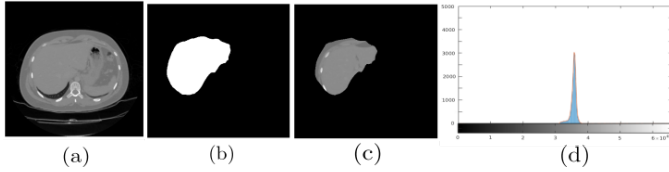


Figure 3: (a)  $P_I$ : largest surface of the liver, (b)  $\bar{M}_{J_k}$ : maximum binary area of the shape model  $\mathbb{M}_k$  with a probability higher than  $\beta_1$ , (c)  $P_I$ : application of  $\bar{M}_{J_k}$  as a mask on  $P_I$ , (d) Intensity histogram of  $P_I$  that allows to determine the mean intensity of the liver

We threshold pixels intensity distribution thanks to the following normality test:

$$\mu - \kappa(\delta)\delta \leq D \leq \mu + \kappa(\delta)\delta, \quad (5)$$

with  $\kappa(\delta) = 34.64 \times \delta^{-0.384}$ .  $\kappa(\delta)$  has a descending exponential form, that allows us to include more pixels in cases with a small value of  $\delta$  ( $\delta$  is the standard deviation of the pixels intensity distribution of  $P_I$ ). The step 1) and the step 2) in Figure 4 show this process.

Finally, we know that the liver is concentrated in the maximum binary area of the shape model chosen so we focus our segmentation only in this delimited area. The localization step is presented in Figure 4 at step 3. That allows us to reduce the influence of the surrounding organs on liver detection.

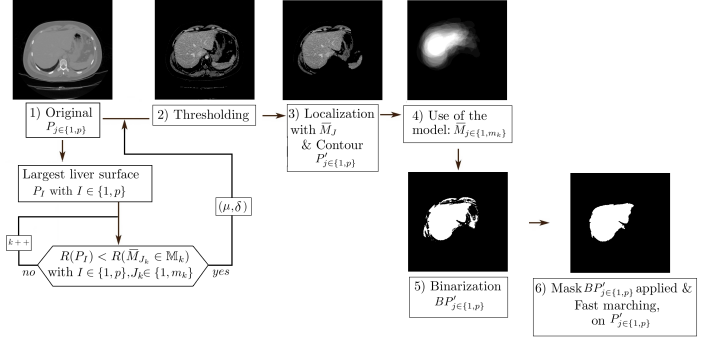


Figure 4: The complete framework to segment volume of liver

### 3.2. Fast marching method and adjustment process

We next apply a smoothing step with an anisotropic diffusion filter using the modified curvature diffusion equation as Draoua *et al.* used in their work [41]. This filter requires three parameters: the number of iterations to be performed ( $n_{it}$ ), the time step ( $t$ ) and the conductance parameter ( $\xi$ ). Then, we compute the magnitude of the gradient by convolution with the first derivative of a Gaussian to detect the contours. We denote the accentuated images contours by  $P'_{j \in \{1, p\}}$  and we binarize these results. Thanks to the process described in the previous section, we know where is the largest area of the patient liver, this information enables us to align the shape model  $\bar{M}_{j \in \{1, m_k\}}$  with the patient data, by the correspondence between  $P_I$  and  $\bar{M}_{J_k}$ . At this step, we can determine the presence of the liver and we choose pixels with a probability higher than a fixed value called  $\beta_2$ . We denote the results by  $BP'_{j \in \{1, p\}}$  (see step 5 in Figure 4). We apply  $BP'_{j \in \{1, p\}}$  as mask on  $P'_{j \in \{1, p\}}$ . Finally, we consider the center of the connected components with pixels having a probability higher than  $\beta_2$  in the shape model and a fast marching method [42] is initialized on images  $P'_{j \in \{1, p\}}$  at this position. The fast marching method solves the Eikonal Equation (6) where the speed  $c(x, y)$  is strictly non-negative and depends on the position  $(x, y)$  only, it means that the front represented by the function  $u$  is always going forward:

$$|\nabla u(x, y)| = \frac{1}{c(x, y)}. \quad (6)$$

The implementation comes from the article [42]. Figure 4 shows the results of these different steps in our algorithm. Our method is implemented with ITK (Insight Segmentation and Registration Toolkit) [43].

We now have a binary 3-D mask of the liver from the medical images  $P_{j \in \{1, p\}}$ ; we denote them by  $MP_{j \in \{1, p\}}$ . The last step consists in erasing the segmentation errors. Indeed, we have calibrated parameters of all the functions used in our method to make them automatic. Therefore the segmentation can be perfect for certain patients but it can also include errors. These errors come from the fast marching method that includes part of the images that do not belong to the liver. In most cases the shape of the liver is Z-convex [44], we use this property to perform the adjustment with  $MP_l$ ,  $l \in \{1, p\}$ , the 2-D mask with the maximum area. Before this slice with the largest area  $MP_l$

of the liver, each surface:  $Surface(MP_j)$  has to be included in the next one:  $Surface(MP_{j+1})$ , so pixels that do not belong to the liver are set to 0 in  $MP_j$ . And after  $l$  slices, each surface  $Surface(MP_j)$  has to be included in the previous one, errors on  $MP_j$  are also solved. Equation (7) and Figure 5 explain this adjustment process:

$$\begin{aligned} \forall j < l, Surface(MP_j) &\subset Surface(MP_{j+1}) \\ \forall j > l, Surface(MP_j) &\subset Surface(MP_{j-1}). \end{aligned} \quad (7)$$

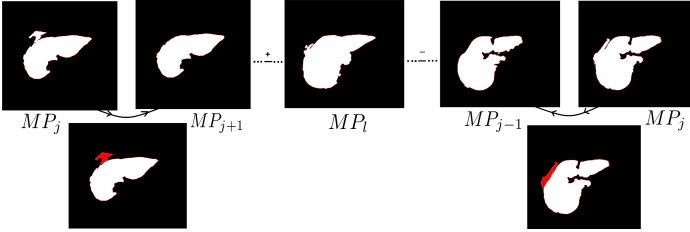


Figure 5: Adjustment to solve segmentation errors: red regions correspond to the difference between two adjacent masks due to over-segmentations

Finally, we have used VTK (Visualization Toolkit) [45] to reconstruct a 3-D representation of the liver. We use the most widely known method of surface extraction: the Marching Cubes algorithm [46]. This method has become a reference in medical imaging processing. Smoothing is also applied on the surface during the process. Figure 6 presents the results of examples from MRI and CT datasets. More experiments are provided at the end of Section 5.

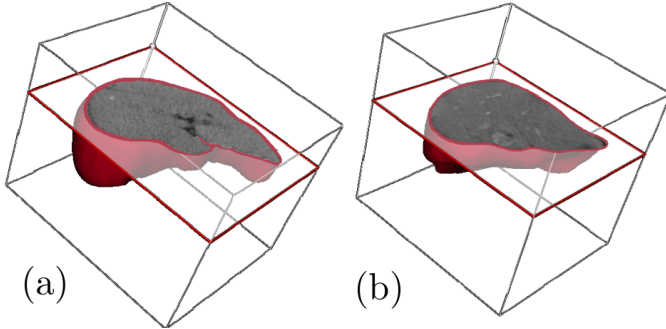


Figure 6: 3-D liver reconstructions on a) MRI and b) CT volumes

#### 4. Measuring robustness

In this article, we also propose to measure the robustness of our contribution, by employing the definition given in [47] extending our previous work [36]. The robustness is not properly and clearly defined in evaluation process of liver segmentation. However, this notion is important because it is related to the concrete use and reproducibility of image processing algorithms [48]. With similar notations as [36, 47], let  $\mathbf{X}$  be the segmentation result of an algorithm,  $\mathbf{Y}^0$  be the ground truth image that should be reached, and  $Q$  a quality measure between them (e.g. Dice coefficient). As in [47], we consider  $m$  scales of

increasing liver variabilities to measure the robustness, denoted by  $\{\sigma_k\}_{1 \leq k \leq m}$ . As a whole, we denote the different outputs of  $A$  for every scale by  $\mathbb{X} = \{\mathbf{X}_k\}_{k=1,m}$ . The ground truth is also denoted by  $\mathbb{Y}^0 = \{\mathbf{Y}_k^0\}_{k=1,m}$ . We now consider the following definition of  $(\alpha, \sigma)$ -robustness:

**Definition 1** ( $(\alpha, \sigma)$ -robustness). *Algorithm A is considered as robust if the difference between the output  $\mathbb{X}$  and ground truth  $\mathbb{Y}^0$  is bounded by a Lipschitz continuity of the  $Q$  function:*

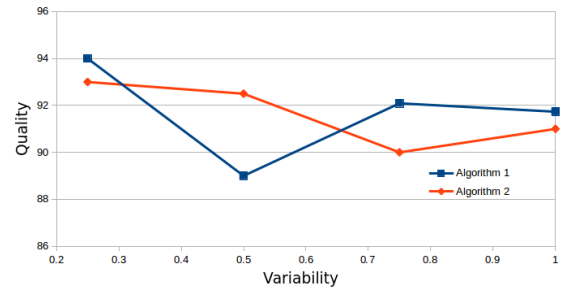
$$d_Y(Q(\mathbf{X}_k, \mathbf{Y}_k^0), Q(\mathbf{X}_{k+1}, \mathbf{Y}_{k+1}^0)) \leq \alpha d_X(\sigma_{k+1}, \sigma_k), \quad 1 \leq k < m,$$

where

$$\begin{aligned} d_Y(Q(\mathbf{X}_k, \mathbf{Y}_k^0), Q(\mathbf{X}_{k+1}, \mathbf{Y}_{k+1}^0)) &= Q(\mathbf{X}_{k+1}, \mathbf{Y}_{k+1}^0) - Q(\mathbf{X}_k, \mathbf{Y}_k^0), \\ d_X(\sigma_{k+1}, \sigma_k) &= |\sigma_{k+1} - \sigma_k|. \end{aligned} \quad (8)$$

We calculate the robustness measure  $(\alpha, \sigma)$  of  $A$  as the  $\alpha$  value obtained and the scale  $\sigma = \sigma_k$  where this value is reached.

In other words, in this definition,  $\alpha$  measures the worst drop in quality through the scales of variability  $\{\sigma_k\}$ , and  $\sigma$  keeps the variability scale leading to this value. The most robust algorithm should have a low  $\alpha$  value, and a very high  $\sigma$  value. Figure 7 illustrates this definition of robustness (compared to previous contribution only measuring  $\alpha$  [36]), applied on a synthetic example of evaluation of two algorithms.



	$\alpha$ (from [36])	$(\alpha, \sigma)$ (from [47])
Algorithm 1	16	(16, 0.25)
Algorithm 2	10	(10, 0.5)

Figure 7: Illustrative example of evaluation of robustness for two algorithms

This example illustrates the better robustness of Algorithm 2, since its  $\alpha$  value is smaller than the one of Algorithm 1. Moreover, we can precise that this robustness is achieved for a larger value of variability with the  $(\alpha, \sigma)$  measurement.

#### 5. Results and discussion

In the first part of the experimentation section, we evaluate our automatic method on both multiple CT and MRI. Then we compare our algorithm with a free available semi-automatic segmentation software, called SmartPaint [37]. As the user intervention is required in this method, we compare different times spent by the user to segment the liver with this semi-automatic method. We also compare our algorithm with similar algorithms, from state of the art. Then, as SLIVER and IRCAD databases are freely available, a lot of studies use them

in their evaluations and are, therefore, directly comparable. Finally, we compare our method with the few studies that propose liver segmentation for both modalities. In the second part of the experimentation section, we compare segmentations obtained with our algorithm and SmartPaint according to the robustness defined in Section 4. To complete our results, we provide 3D illustrations of CT and MRI volumes resulting from our algorithm. We show results on standard and dysmorphic liver shapes (livers are deformed by diseases such as cirrhosis and/or tumors).

### 5.1. Experiments and comparisons

Parameters used for CT and MRI to segment the liver, are presented in Table 1. Then, quantitative results from applying our method to segment the liver on the CT and MRI volumes are presented in Table 2. Our automatic method and experts manual segmentations of liver segmentation, are compared by widely, and suitable metrics designed to quantify the accuracy. We use the True Positive (TP) and False Negative (FN) rates in range 0 to 1 to evaluate the REcall value (RE), the PREcision value (PRE), the Jaccard index (J) and the Dice coefficient (D). For the IRCAD and SLIVER databases, manual segmentations are available for all CT scans. Our algorithm has been applied to the forty MRI volumes and currently we have three available manual segmentations. We obtain a Dice value equals to 88% for IRCAD dataset, 93% for SLIVER and 90% for MRI images.

Parameters	$n_{it}$	$t$	$\xi$	$\beta_1$ (%)	$\beta_2$ (%)
Values	5	0.1	1	30	30

Table 1: Fixed parameters for the fast marching steps and probability used to segment the liver are listed with their corresponding values

Dataset	RE	J	D
IRCAD	0.87±0.05	0.78±0.06	0.88±0.03
SLIVER	0.92±0.03	0.87±0.04	0.93±0.02
MRI	0.91±0.08	0.82±0.04	0.90±0.02
	FN	TP	PRE
IRCAD	0.13±0.05	0.85±0.07	0.89±0.04
SLIVER	0.08±0.03	0.92±0.03	0.94±0.03
MRI	0.09±0.07	0.90±0.10	0.88±0.06

Table 2: Evaluation results of liver segmentation accuracy on CT and on MRI

In this section, we compare our model with a semi-automatic method, where the intervention of the user is essential. This method, called SmartPaint [37], allows an interactive segmentation of medical volume images based on region growing. Other quantitative comparisons are proposed at the end of this section. With SmartPaint, the user performs liver and background localizations and to help in a second step the interactive delineation of the organ of interest by the algorithm. The liver is segmented by "sweeping" with the mouse cursor in the image, and the user adds or removes details in 2-D or 3-D by the proposed segmentation tool. For the comparison, an operator, skilled in biomedical image processing, who had received a short training on liver anatomy, but was not a radiological expert, performed

liver segmentations on the SLIVER training dataset. We first begin by a coarse segmentation in 3-D and we refine it in 2-D, slice by slice to solve some errors caused by region growing. With SmartPaint, the user can seamlessly adjust the trade-off between image-content assisted and completely manual segmentation, ensuring the ability to produce any segmentation result with enough interaction time. In this context, we decided to evaluate two times of the user interaction: 5 and 15 min. In a previous evaluation of SmartPaint, where interactive segmentation was performed by an operator who had received training on the liver anatomy, but was not a radiological expert, the average operator time required for liver segmentation was 10 minutes and 18 seconds [37]. SmartPaint is currently ranked 20/108 in the SLIVER Challenge. Results are presented in Table 3 on a set of four CT volumes from SLIVER database. We notice that SmartPaint gives significant results with 86% for the Dice coefficient and does not consume a lot amount of time, with equivalent results for 5 minutes and 15 minutes. However our automatic segmentation outperforms the user dependent method with a Dice coefficient equals to 95%.

SLIVER ( $N = 4$ )	RE	J	D
SmartPaint (5min)	0.80±0.05	0.75±0.06	0.86±0.04
SmartPaint (15min)	0.77±0.02	0.76±0.03	0.86±0.02
Our method	0.94±0.02	0.90±0.01	0.95±0.01
	FN	TP	PRE
SmartPaint (5min)	0.24±0.05	0.82±0.05	0.93±0.02
SmartPaint (15min)	0.23±0.02	0.86±0.12	0.95±0.03
Our method	0.06±0.02	0.93±0.01	0.96±0.02

Table 3: Comparison with SmartPaint with different times on CT-volumes

SLIVER	RE	J	D
SmartPaint	0.85±0.07	0.82±0.06	0.90±0.04
Our method	0.92±0.03	0.87±0.04	0.93±0.02
	FN	TP	PRE
SmartPaint	0.14±0.07	0.87±0.07	0.95±0.04
Our method	0.08±0.03	0.92±0.03	0.94±0.03
MRI	RE	J	D
SmartPaint	0.91±0.05	0.87±0.06	0.91±0.04
Our method	0.91±0.08	0.82±0.04	0.90±0.02
	FN	TP	PRE
SmartPaint	0.08±0.04	0.92±0.09	0.94±0.05
Our method	0.09±0.07	0.90±0.10	0.88±0.06

Table 4: Comparison of segmentation on the SLIVER datasets and MRI from our database

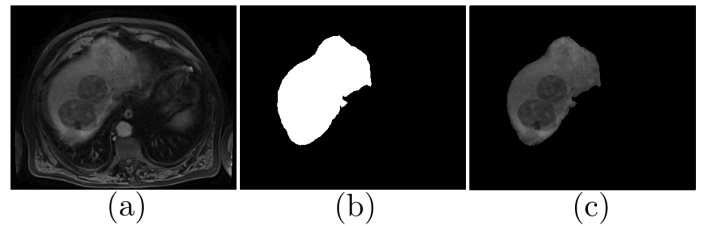


Figure 8: Visual results on an MRI with HCC: (a) Medical exam with HCC, (b) Mask from our algorithm, (c) Application of the mask

As user time interaction is not significant, we compare segmentations done by SmartPaint and by our method on the 20 SLIVER training images without considering time of interaction. We obtain 93% with our algorithm for the Dice coefficient and 90% with SmartPaint, Table 4 shows the results. SmartPaint is not time dependent and our automatic method is better than the semi-automatic method. We also evaluate our method and SmartPaint on three MRI volumes. Due to the significant noise, complex inhomogeneous background, partial volume effects and image resolution, segmentation on MRI is a challenging task. Moreover, MRI volumes come from patients with advanced cirrhosis, and the disease severely deforms their livers (see Figure 8). Despite these difficulties, results obtained with our method are similar to a method with the user intervention requiring a mean Dice value equals to 90%.

Now, we compare our method with three automatic algorithms based on statistical models tested on CT scans different from the SLIVER dataset. Massoptier *et al.* [15] obtain 94% for the Dice coefficient. We get 93% for the whole SLIVER dataset, we are close to their performance but our method consumes less time. In their article, an average computational time of 11.4 s is requested for processing a  $512 \times 512$  pixels slice, while our method requests 5-6 s for same dimensions. A manual expert segmentation generally requires 3-4 min for one slice [49]. Okada *et al.* [26] obtain a Jaccard coefficient equals to 86% for 8 CT scans; we obtain 87% for the 20 SLIVER training images. Farzaneh *et al.* [16] obtain a Dice coefficient higher than 89% on 11 similar images in pixel spacing. The mean Dice coefficient in our study is 90.5% for 40 different datasets and our algorithm also work on MRI images.

Then, the CT databases: SLIVER and IRCAD allow a direct comparison with other methods. Linguraru *et al.* [25] obtain a Dice value equal to 96% on the SLIVER dataset. However, our computation time, 5-6 seconds, is better than their Atlas based method which request 3000-3600 seconds per slice. Then our results are less performant than methods of the articles [13, 24, 27, 50, 51], however all of them concentrate their task only on CT scans. These methods are limited in case of reconstruction accuracy on diseased livers involving large deformations and lesions. Moreover, process in the article [13] is user-dependent. The advantage is that our method is fully automatic, generic and also works on MRI with promising results whatever the liver disease. Deep learning on CT scans is more accurate than our method [28, 29] but we also segment liver on MRI. Then, our results on MRI are similar to those of Shin *et al.* [30] who use deep learning on MRI, with a recall value of 0.91 (see Table 2); however they do not test their method on CT scans.

As far as we know, it does not exist free available database with manual segmentation of the liver on MRI except the database called Visceral [52]. However, data are presented as part of a Benchmarking which has reached an end in 2017, and data seem no more accessible. Nonetheless their segmentation results leaderboard shows a study with a maximum Dice equal to 90.2% on MRI for the Computer Vision Lab, ETH Zurich and 95% on CT for Creatis, INSA-LYON. Our results are sim-

ilar but we produce one algorithm for both modalities MRI and CT. Then, lot of studies use private data that makes comparison a difficult task, yet we present some results.

Finally, Table 5 presents studies where CTs and MRI are both used. Few liver segmentation methods for both modalities have been reported; we compare ours with the most recent [31, 32, 33, 34]. We are close to their performances but methods of Gotra *et al.* [31], Chartrand *et al.* [32] and Suzuki *et al.* [33] are user-dependent and ours is automatic. The framework presented by Gotra *et al.* [31] has two user tasks, a liver delineation and a manipulation of surface mesh. Patients are the same for CT and MRI that limits the variability of the liver shape. The method presented in [32] needs an initialization of the contours by the user. Then, in the article [33] some parameters are fixed by the user. Our results are better than results obtained by Heinrich *et al.* [34] who present an atlas registration for CTs and MRI data. Finally, our results are better on MRI than recent automatic method presented by Chris *et al.* [35].

Method	Ref	CT			MRI		
		Data	D	J	Data	D	J
Auto	Ours	SLIVER	93	87	private	90	87
		IRCAD	88	78			
Semi-Auto	[33] 2015	private	93		private	93	
Semi-Auto	[31] 2017	private		90	private		88
Semi-Auto	[32] 2017	SLIVER		94	private		92
Auto	[34] 2015	private	92		private	80	
Auto	[35] 2017	private	91	84	private	87	77
		IRCAD	94.3	89.3			

Table 5: Comparison with other semi-automatic and automatic methods on SLIVER and CT or MRI private datasets

## 5.2. Robustness

Now, we compare segmentations obtained from CT volumes (IRCAD and SLIVER) with our algorithm and with SmartPaint, according to their variabilities defined in Section 2.2.

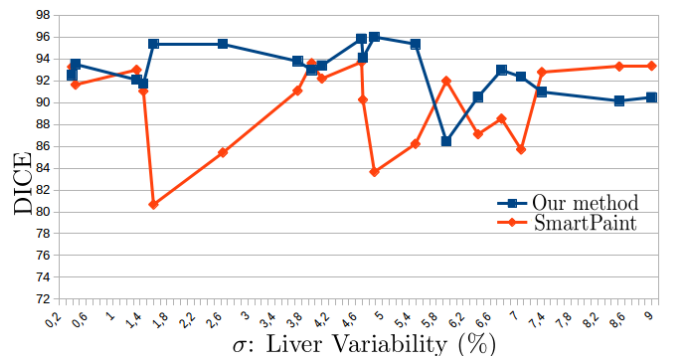


Figure 9: Performance of our algorithm according to liver's shape

SLIVER	Std (%)	$\alpha$ [36]	$(\alpha, \sigma)$ [47]
SmartPaint	4	19.4	(19.4, 5.49)
Our method	2	73.5	(73.5, 4.71)

Table 6: Evaluation of robustness for our approach, compared to SmartPaint

Figure 9 shows the performance of our algorithm according to this variability  $\sigma_M$  defined in Equation (1) and Table 6 summarizes quantitative evaluation of robustness (see Section 4). In this Table 6, the standard deviation of Dice measure over the whole dataset is 2% for our method and 4% for SmartPaint; our algorithm is thus more stable than SmartPaint. Moreover, we show the robustness of our approach compared to SmartPaint, with the same definitions as [36] ( $\alpha$  value) and with measure  $(\alpha, \sigma)$  [47]. These evaluations show that the output of our approach can be altered with lower damage than for SmartPaint, and with a more difficult case. As a consequence, we can observe that our contribution is more robust than SmartPaint, over a large dataset. The code providing this robustness evaluation, and the synthetic example depicted in Figure 7 is publicly downloadable<sup>1</sup>. Our algorithm is thus able to resist the perturbation due to the variability of the liver shape (Figure 6).

### 5.3. 3-D Representation

In this section, we provide illustrations of the results of our algorithm on both modalities CT and MRI. Figures 12 and 13 provide results of the 3-D liver segmentation algorithm obtained on CT and MRI volumes. Some livers are more easy to segment due to images quality, high contrast of images, standard shape of the liver and homogeneous intensities. For instance, MRI is more difficult to segment than CT scans due to the quality of the images. Moreover, our MRI volumes correspond to livers with tumors or/and advanced cirrhosis. Therefore the organ is dysmorphic with irregular contours which makes the segmentation task more difficult. We decided to show for each modality (CT and MRI) a segmentation of a standard patient liver volume and a complicated case with an atypical liver shape in Figures 12 and 13. For each case, typical and atypical, we show for one original image of the patient (a), the liver mask obtained from our algorithm (b) and the segmentation (c). With this segmentation, we can construct the 3-D volume without intermediary functions, two different views are presented (d). Then we apply a filter that adjusts point coordinates using Laplacian smoothing [53]. The effect is to "relax" the mesh, making the cells better shaped and the vertices more evenly distributed [45]. Figures 12 (e) and 13 (e) show screenshot of an ITK-VTK code that we developed to interactively visualize the result of the liver segmentation with our method after the application of a triangle mesh decimation and a smoothing filter. It allows to see the liver in 3-D in different positions and to define a plane that can be interactively placed in the image volume. Finally, we show two different views of the isosurface of the liver in red colour (f). We perform this surface extraction using an algorithm similar to Marching Cubes [43]. Figures 10 and 11 present ten isosurfaces of CT scans and ten isosurfaces of MRI volumes respectively, with different difficulty levels as mentioned previously. A video on 3-D smooth representations of a patient liver (CT scans) is available on the following website: <https://youtu.be/mHPU-cCuTBw>.

<sup>1</sup><https://github.com/antoinevacavant/robustimageprocessing>

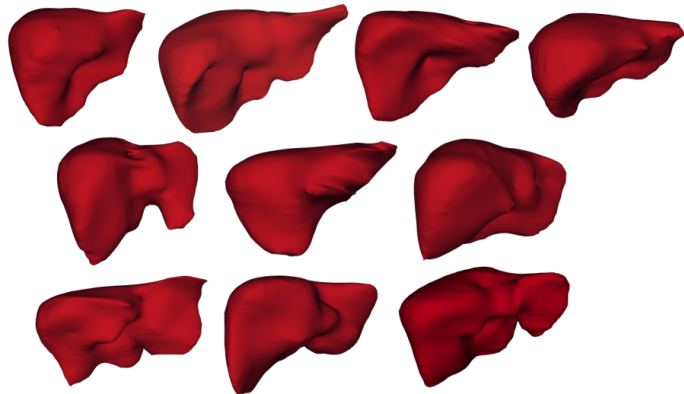


Figure 10: Isosurfaces of CT scans

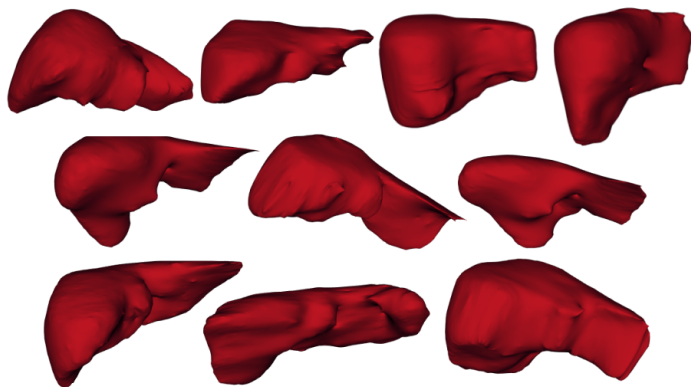


Figure 11: Isosurfaces of MRI volumes

## 6. Conclusion

In this article, we present an automatic segmentation algorithm of the liver on CT and MRI images from different machines by using a model based on the variabilities of the liver. We first normalize all the datasets to treat different images (1 mm for pixel spacing), then our algorithm is automatically adapted to the processed image. The model based on the liver shape variability, constructed thanks to expert segmentations, enables to locate the liver on medical images, compute a threshold to isolate it and initialize an active contour method. Our algorithm takes into account the liver shape variability and it leads to a 3-D reconstruction for CT and MRI volumes. It can be used to process any medical image by overcoming the parametric constraints imposed by the machines. We obtain a mean Dice equal to 90.5% for CT volumes and 90% for MRI. In our study we present a generic method with a compromise between the performance, the computation time, the diversity and the quantity of the data (MRI and large free available CT-datasets). Using our definition of robustness, we have also shown that our contribution can resist to the variability of this so complex organ. We currently work on different MRI acquisition

times (portal, arterial, diffusion, *etc.*); we employ 3-D reconstruction of these dynamic MRI volumes to develop a method to detect tumors automatically as radiologists do with visual criteria based on the different acquisition times. Moreover our method can be applied to other solid organs: kidneys or pancreas for instance, to do this, we need expert segmentation to build a multi-variability model. The method can be extended to other applications to isolate an element, if *a priori* knowledge of the shape of the object is available. Thanks to this liver segmentation we are already able to detect hepatic tumor as hepatocellular carcinoma [54]. The next step of this article is to extract the vascular network in 3-D [55] to study the blood flow and locate the onset of possible dysfunctions, as we already started in [56]. This investigation will also improve the evaluation of the robustness of image segmentation algorithm [57], as the simulation becomes a relevant way to assess the quality of the extraction of regions of interest (liver parenchyma, vessels and tumors) from medical images.

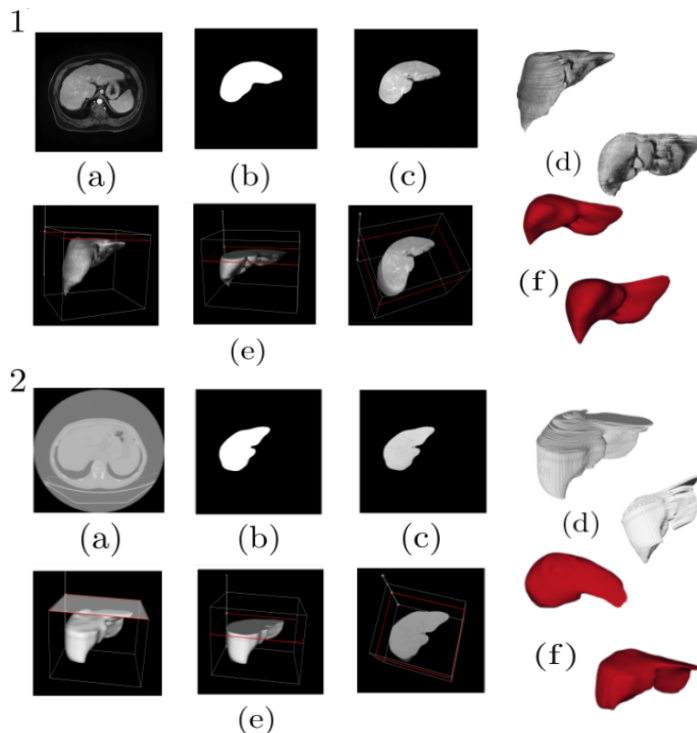


Figure 13: Visual results on 1) typical and 2) atypical MRI volume: (a) Patient image, (b) Mask of the liver, (c) Final segmentation, (d) 3-D liver representation with raw data, (e) Smooth 3-D representations, (f) Isosurface

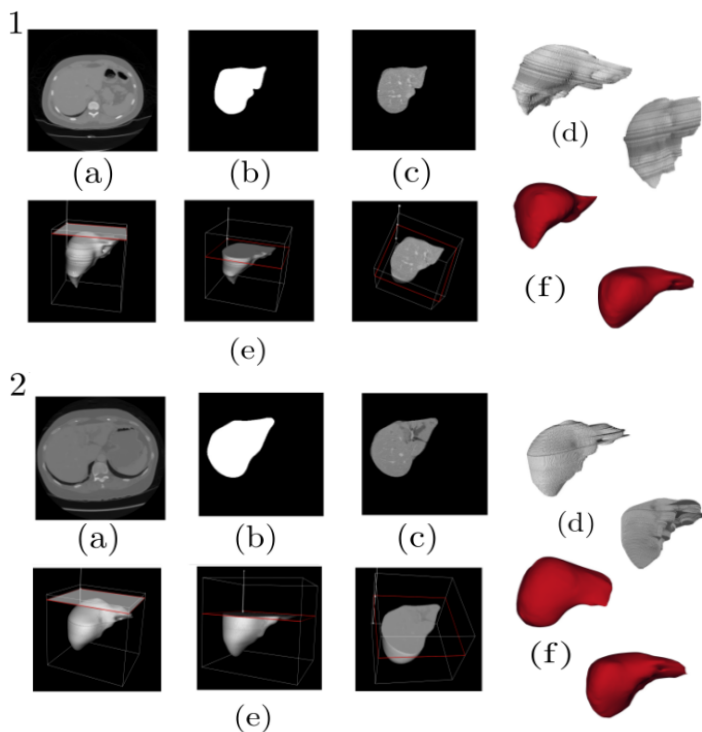


Figure 12: Visual results on 1) typical and 2) atypical CT volume: (a) Patient image, (b) Mask of the liver, (c) Final segmentation, (d) 3-D liver representation with raw data, (e) Smooth 3-D representations, (f) Isosurface

## 7. References

- [1] L. Ruskó, G. Bekes, M. Fidrich, Automatic segmentation of the liver from multi-and single-phase contrast-enhanced CT images, *Medical Image Analysis* 13 (6) (2009) 871–882.
- [2] R. Yuan, M. Luo, S. Wang, L. Wang, Q. Xie, A method for automatic liver segmentation from multi-phase contrast-enhanced CT images, *Medical Imaging 2014: Computer-Aided Diagnosis* 9035 (2014) 90353H.
- [3] A. H. Foruzan, R. A. Zoroofi, M. Hori, Y. Sato, Liver segmentation by intensity analysis and anatomical information in multi-slice CT images, *International journal of computer assisted radiology and surgery* 4 (3) (2009) 287–297.
- [4] S.-J. Lim, Y.-Y. Jeong, Y.-S. Ho, Automatic liver segmentation for volume measurement in CT images, *Journal of Visual Communication and Image Representation* 17 (4) (2006) 860–875.
- [5] P. Campadelli, E. Casiraghi, S. Pratisoli, G. Lombardi, Automatic abdominal organ segmentation from CT images, *ELCVIA: electronic letters on computer vision and image analysis* 8 (1) (2009) 1–14.
- [6] J. Peng, D. Kong, F. Dong, A new adaptive variational model for liver segmentation with region appearance propagation, *Preprint* (2011) 4–7.
- [7] C. Shi, Y. Cheng, F. Liu, Y. Wang, J. Bai, S. Tamura, A hierarchical local region-based sparse shape composition for liver segmentation in CT scans, *Pattern Recognition* 50 (2016) 88–106.
- [8] F. Liu, B. Zhao, P. K. Kijewski, L. Wang, L. H. Schwartz, Liver segmentation for CT images using gvf snake, *Medical physics* 32 (12) (2005) 3699–3706.
- [9] E. Göçeri, M. Z. Ünlü, O. Dicle, A comparative performance evaluation of various approaches for liver segmentation from SPIR images, *Turkish Journal of Electrical Engineering & Computer Sciences* 23 (3) (2015) 741–768.
- [10] E. Göçeri, M. N. Gürçan, O. Dicle, Fully automated liver segmentation from SPIR image series, *Computers in biology and medicine* 53 (2014) 265–278.

- [11] E. Göçeri, Fully automated liver segmentation using Sobolev gradient-based level set evolution, *International journal for numerical methods in biomedical engineering* 32 (11) (2016) e02765.
- [12] L. Soler, H. Delingette, G. Malandain, J. Montagnat, N. Ayache, C. Koehl, O. Dourthe, B. Malassagne, M. Smith, D. Mutter, Fully automatic anatomical, pathological, and functional segmentation from CT scans for hepatic surgery, *Computer Aided Surgery* 6 (3) (2001) 131–142.
- [13] X. Yang, H. C. Yu, Y. Choi, W. Lee, B. Wang, J. Yang, H. Hwang, J. H. Kim, J. Song, B. H. Cho, et al., A hybrid semi-automatic method for liver segmentation based on level-set methods using multiple seed points, *Computer methods and programs in biomedicine* 113 (1) (2014) 69–79.
- [14] A. Brunton, A. Salazar, T. Bolkart, S. Wuhrer, Statistical shape spaces for 3d data: A review, *Handbook of Pattern Recognition and Computer Vision* (2015) 217.
- [15] L. Massoptier, S. Casciaro, A new fully automatic and robust algorithm for fast segmentation of liver tissue and tumors from CT scans, *European radiology* 18 (8) (2008) 1658.
- [16] N. Farzaneh, S. Samavi, S. R. Soroushmehr, H. Patel, S. Habbo-Gavin, D. P. Fessell, K. R. Ward, K. Najarian, Liver segmentation using location and intensity probabilistic atlases, *International Conference of the IEEE Engineering in Medicine and Biology Society (EMBC)* (2016) 6453–6456.
- [17] T. F. Cootes, C. J. Taylor, et al., Statistical models of appearance for medical image analysis and computer vision, *Medical Imaging 2001: Image Processing* 4322 (236-248) (2001) 5.
- [18] T. F. Cootes, G. J. Edwards, C. J. Taylor, et al., Comparing active shape models with active appearance models, *The British Machine Vision Conference (BMVC)* 99 (1) (1999) 173–182.
- [19] P. Dreuw, T. Deselaers, D. Keysers, H. Ney, Modeling image variability in appearance-based gesture recognition, *European Conference on Computer Vision Workshop on Statistical Methods in Multi-Image and Video Processing* (2006) 7–18.
- [20] D. Merck, G. Tracton, R. Saboo, J. Levy, E. Chaney, S. Pizer, S. Joshi, Training models of anatomic shape variability, *Medical physics* 35 (8) (2008) 3584–3596.
- [21] K. Rodzik, D. Sawicki, Recognition of the human fatigue based on the icaam algorithm, *International Conference on Image Analysis and Processing* (2015) 373–382.
- [22] Š. Iveković, A. Leonardis, Multiresolution approach to biomedical image segmentation with statistical models of appearance, *International Conference on Scale-Space Theories in Computer Vision* (2003) 667–682.
- [23] B. He, C. Huang, G. Sharp, S. Zhou, Q. Hu, C. Fang, Y. Fan, F. Jia, Fast automatic 3d liver segmentation based on a three-level adaboost-guided active shape model, *Medical physics* 43 (5) (2016) 2421–2434.
- [24] A. Wimmer, J. Hornegger, G. Soza, Implicit active shape model employing boundary classifier, *2008 19th International Conference on Pattern Recognition* (2008) 1–4.
- [25] M. G. Linguraru, J. K. Sandberg, Z. Li, F. Shah, R. M. Summers, Automated segmentation and quantification of liver and spleen from CT images using normalized probabilistic atlases and enhancement estimation, *Medical physics* 37 (2) (2010) 771–783.
- [26] T. Okada, R. Shimada, M. Hori, M. Nakamoto, Y. Chen, H. Nakamura, Y. Sato, Automated segmentation of the liver from 3-D CT images using probabilistic atlas and multilevel statistical shape model, *Academic radiology* 15 (11) (2008) 1390–1403.
- [27] M. Moghbel, S. Mashohor, R. Mahmud, M. I. B. Saripan, Automatic liver segmentation on computed tomography using random walkers for treatment planning, *Experimental and Clinical Sciences, International Online Journal for Advances in Sciences* 15 (2016) 500.
- [28] Q. Dou, H. Chen, Y. Jin, L. Yu, J. Qin, P.-A. Heng, 3-D deeply supervised network for automatic liver segmentation from CT volumes, *International Conference on Medical Image Computing and Computer-Assisted Intervention* (2016) 149–157.
- [29] P. Hu, F. Wu, J. Peng, P. Liang, D. Kong, Automatic 3-D liver segmentation based on deep learning and globally optimized surface evolution, *Physics in Medicine and Biology* 61 (24) (2016) 8676.
- [30] H.-C. Shin, M. R. Orton, D. J. Collins, S. J. Doran, M. O. Leach, Stacked autoencoders for unsupervised feature learning and multiple organ detection in a pilot study using 4-D patient data, *IEEE Transactions on Pattern Analysis and Machine Intelligence* 35 (8) (2013) 1930–1943.
- [31] A. Gotra, G. Chartrand, K.-N. Vu, F. Vandenbroucke-Menu, K. Massicotte-Tisluck, J. A. de Guise, A. Tang, Comparison of MRI-and CT-based semiautomated liver segmentation: a validation study, *Abdominal Radiology* 42 (2) (2017) 478–489.
- [32] G. Chartrand, T. Cresson, R. Chav, A. Gotra, A. Tang, J. A. De Guise, Liver segmentation on ct and mr using laplacian mesh optimization, *IEEE Transactions on Biomedical Engineering* 64 (9) (2017) 2110–2121.
- [33] K. Suzuki, H. T. Huynh, Y. Liu, D. Calabrese, K. Zhou, A. Oto, M. Hori, Computerized segmentation of liver in hepatic CT and MRI by means of level-set geodesic active contouring, *35th Annual International Conference of the IEEE Engineering in Medicine and Biology Society (EMBC)* (2013) 2984–2987.
- [34] M. P. Heinrich, O. Maier, H. Handels, Multi-modal multi-atlas segmentation using discrete optimisation and self-similarities, *VISCERAL Challenge, IEEE International Symposium on Biomedical Imaging* (2015) 27–30.
- [35] P. F. Christ, F. Ettliger, F. Grün, M. E. A. Elshaera, J. Lipkova, S. Schlecht, F. Ahmaddy, S. Tatavarty, M. Bickel, P. Bilic, et al., Automatic liver and tumor segmentation of CT and MRI volumes using cascaded fully convolutional neural networks, *arXiv preprint arXiv:1702.05970* (2017).
- [36] A. Vacavant, A novel definition of robustness for image processing algorithms, *Workshop on Reproducible Research in Pattern Recognition of the International Conference on Pattern Recognition* 10214 (2016) 75–87.
- [37] F. Malmberg, R. Nordenskjöld, R. Strand, J. Kullberg, Smartpaint: a tool for interactive segmentation of medical volume images, *Computer Methods in Biomechanics and Biomedical Engineering: Imaging and Visualization* 5 (1) (2017) 36–44.
- [38] M. Kistler, S. Bonaretti, M. Pfahrer, R. Niklaus, P. Büchler, The virtual skeleton database: An open access repository for biomedical research and collaboration, *Journal of medical Internet research* (2013) 15 (11). <http://www.ircad.fr/research/3d-ircadb-01/>, 2018.
- [40] T. Heimann, B. Van Ginneken, M. A. Styner, Y. Arzhaeva, V. Aurich, C. Bauer, A. Beck, C. Becker, R. Beichel, G. Bekes, Comparison and evaluation of methods for liver segmentation from CT datasets, *IEEE Transactions on Medical Imaging* (2009) 28 (8).
- [41] A. Draoua, A. Albouy-Kissi, A. Vacavant, V. Sauvage, A new iterative method for liver segmentation from perfusion CT scans, *Medical Imaging 2014: Image Perception, Observer Performance, and Technology Assessment* 9037 (2014) 90371P.
- [42] J. A. Sethian, *Level set methods and fast marching methods: evolving interfaces in computational geometry, fluid mechanics, computer vision, and materials science*, Cambridge university press (1999).
- [43] T. S. Yoo, M. J. Ackerman, W. E. Lorensen, W. Schroeder, V. Chalana, S. Aylward, D. Metaxas, R. Whitaker, Engineering and algorithm design for an image processing API: a technical report on ITK-the insight toolkit, *Studies in health technology and informatics* (2002) 586–592.
- [44] C. E. Kim, A. Rosenfeld, Digital straight lines and convexity of digital regions, *IEEE Transactions on Pattern Analysis and Machine Intelligence* (2) (1982) 149–153.
- [45] W. Schroeder, K. Martin, B. Lorensen, *The visualization toolkit, Kitware, VTK* (2003).
- [46] W. E. Lorensen, H. E. Cline, Marching cubes: A high resolution 3-D surface construction algorithm, *International Association for Computing Machinery's Special Interest Group on Computer Graphics and Interactive Techniques* 21 (4) (1987) 163–169.
- [47] A. Vacavant, M.-A. Lebre, H. Rositi, M. Grand-Brochier, R. Strand, New definition of quality-scale robustness for image processing algorithms, with generalized uncertainty modeling, applied to denoising and segmentation, *Workshop on Reproducible Research in Pattern Recognition of the International Conference on Pattern Recognition* (2018) 11455, to appear.
- [48] B. Kerautret, M. Colom, P. Monasse, *Reproducible Research in Pattern Recognition: First International Workshop, 2016, Cancún, Mexico, December 4, 2016, Revised Selected Papers* 10214, (2017).
- [49] L. Hermoye, I. Laamari-Azjal, Z. Cao, L. Annet, J. Lerut, B. M. Dawant, B. E. Van Beers, Liver segmentation in living liver transplant donors: comparison of semiautomatic and manual methods, *Radiology* 234 (1) (2005) 171–178.
- [50] X. Zhang, J. Tian, K. Deng, Y. Wu, X. Li, Automatic liver segmentation using a statistical shape model with optimal surface detection, *IEEE Transactions on Biomedical Engineering* 57 (10) (2010) 2622–2626.
- [51] T. Heimann, S. Münzing, H.-P. Meinzer, I. Wolf, A shape-guided de-

formable model with evolutionary algorithm initialization for 3-D soft tissue segmentation, Biennial International Conference on Information Processing in Medical Imaging (2007) 1–12.

- [52] O. A. Jiménez-del Toro, A. Hanbury, G. Langs, A. Foncubierta-Rodríguez, H. Müller, Overview of the VISCERAL retrieval benchmark 2015, in: *Multimodal retrieval in the medical domain*, Springer, (2015), pp. 115–123.
- [53] G. Taubin, T. Zhang, G. Golub, Optimal surface smoothing as filter design, *European Conference on Computer Vision* (1996) 283–292.
- [54] A. L. M. Pavan, M. Benabdallah, M.-A. Lebre, D. Rodrigues de Pina, A. Mtibaa, A. Vacavant, A parallel framework for HCC Detection in DCE-MRI sequences with wavelet-based description and SVM classification, *Proceedings of the 33rd Annual ACM Symposium on Applied Computing* (2018) 14–21.
- [55] M.-A. Lebre, A. Vacavant, M. Grand-Brochier, B. Magnin, A. Abergel, P. Chabrot, Automatic 3-D skeleton-based segmentation of liver vessels from MRI and CT for Couinaud representation, *IEEE International Conference on Image Processing* (2018) 3523–3527.
- [56] M.-A. Lebre, K. Arrouk, A.-K. Vo Van, A. Leborgne, M. Grand-Brochier, P. Beaurepaire, A. Vacavant, B. Magnin, A. Abergel, P. Chabrot, Medical image processing and numerical simulation for digital hepatic parenchymal blood flow, *International Workshop on Simulation and Synthesis in Medical Imaging* (2017) 99–108.
- [57] A. Vacavant, *Robust image processing: Definition, algorithms and evaluation*, Habilitation in computer science, Université Clermont Auvergne, (2018).